

Hematoporphyrin–ZnO Nanohybrids: Twin Applications in Efficient Visible-Light Photocatalysis and Dye-Sensitized Solar Cells

Soumik Sarkar,[†] Abhinandan Makhal,[†] Tanujjal Bora,[‡] Karthik Lakhsman,[‡] Achintya Singha,[∇] Joydeep Dutta,^{‡,§} and Samir Kumar Pal^{*,†}

[†]Department of Chemical, Biological and Macromolecular Sciences, S. N. Bose National Centre for Basic Sciences, Block JD, Sector III, Salt Lake, Kolkata 700 098, India

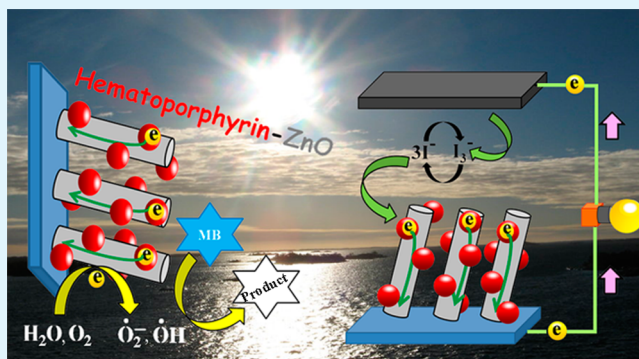
[‡]Centre of Excellence in Nanotechnology, School of Engineering and Technology, Asian Institute of Technology, Klong Luang, Pathumthani 12120, Thailand

[§]Chair in Nanotechnology, Water Research Center, Sultan Qaboos University, PO Box 17, 123 Al-Khoudh, Sultanate of Oman

[∇]Department of Physics, Bose Institute, 93/1, Acharya Prafulla Chandra Road, Kolkata 700 009, India

ABSTRACT: Light-harvesting nanohybrids (LHNs) are systems composed of an inorganic nanostructure associated with an organic pigment that have been exploited to improve the light-harvesting performance over individual components. The present study is focused on developing a potential LHN, attained by the functionalization of dense arrays of ZnO nanorods (NRs) with a biologically important organic pigment hematoporphyrin (HP), which is an integral part of red blood cells (hemoglobin). Application of spectroscopic techniques, namely, Fourier transform infrared spectroscopy (FTIR) and Raman scattering, confirm successful monodentate binding of HP carboxylic groups to Zn²⁺ located at the surface of ZnO NRs. Picosecond-resolved fluorescence studies on the resulting HP–ZnO nanohybrid show efficient electron migration from photoexcited HP to the host ZnO NRs. This essential photoinduced event activates the LHN under sunlight, which ultimately leads to the realization of visible-light photocatalysis (VLP) of a model contaminant Methylene Blue (MB) in aqueous solution. A control experiment in an inert gas atmosphere clearly reveals that the photocatalytic activity is influenced by the formation of reactive oxygen species (ROS) in the media. Furthermore, the stable LHNs prepared by optimized dye loading have also been used as an active layer in dye-sensitized solar cells (DSSCs). We believe these promising LHNs to find their dual applications in organic electronics and for the treatment of contaminant wastewater.

KEYWORDS: hematoporphyrin, light-harvesting nanohybrids, photoinduced electron transfer, visible-light photocatalysis, reactive oxygen species, porphyrin-sensitized solar cell



1. INTRODUCTION

Light-harvesting nanohybrids (LHNs) are of intense current interest, as the simple search for individual nanoparticles no longer incites broad scientific interests for specific high-end applications. Most of these LHNs are composed of an inorganic nanostructure associated with an organic pigment. For example, association of a ruthenium-based sensitizing dye (SD) N719 with TiO₂ or ZnO nanomaterials leads to very efficient LHNs for dye-sensitized solar cell (DSSC) applications.^{1–4} The cost, rarity, and environmental issues of ruthenium complexes limit their wide application and encourage exploration of less-expensive, stable, and safer sensitizers. In this respect, porphyrin and porphyrin derivatives have shown promise for the replacement of ruthenium-based dyes for cost-effective and steady photovoltaic conversion of solar energy to electrical energy, because of their strong absorption in the region of 400–450 nm (B or Soret band) as well as 500–700 nm (Q

bands). Several types of model porphyrins have been synthesized and their photophysical and electrochemical properties at the organic dye-semiconductor interface has been intensively studied.^{5–20} These reports have revealed that the efficiency of porphyrin-sensitized solar cells can be increased by adding donor groups to the porphyrin ring, attaching bulky substituents to the phenyl groups, or by introducing double or triple bonds between the porphyrin ring and the anchoring carboxylic group (COOH). For example, Yalla et al. introduced long alkoxy groups into the porphyrin ring and achieved an unprecedented 12.3% energy conversion efficiency in combination with a cobalt-based electrolyte and a complementary dye Y123.²¹ More recently, boron dipyrrome-

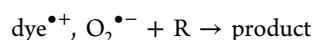
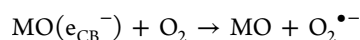
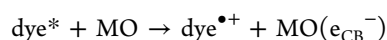
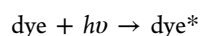
Received: October 11, 2012

Accepted: November 27, 2012

Published: November 27, 2012

these compound has been synthesized and coadsorbed on TiO₂ nanoparticles with porphyrin dyes, which lead to a significant enhancement of energy conversion efficiency.¹¹

Along with successful recognition of efficient DSSCs, harvesting solar energy has also attracted a lot of attention to reduce organic pollutants at very low concentration by means of visible-light photocatalysis (VLP). In both applications, the basic building block is a sensitizer, which absorbs visible light from the sun, thereby initiating electron migration upon photoexcitation. The decisive use of various sensitizers including quantum dots in the system is found to be one of the key considerations in the realization of resourceful LHNs for efficient electron migration from sensitizers to the nanoparticulate film of a wide-band-gap oxide semiconductor, and eventually the charge separation determines the VLP activity and the quality of DSSCs.²² In this respect, because of its large band gap (3.3 eV), the popular photocatalyst ZnO can only utilize ~4% of the incoming solar energy, thus restricting its practical applications in a model VLP process. Therefore, a visible-light-activated catalyst is desired that can take the benefit of utilizing a superior portion of the solar spectrum and would be much more effective in ecological cleanup. In the viewpoint of effective utilization of visible solar radiation, efforts have been made to trigger a photocatalyst under visible light by extending its photoresponse to the visible region by metal-ion doping,²³ nonmetal doping,^{24,25} noble-metal deposition,²⁶ narrow-band-gap semiconductors coupling,^{27–29} conducting polymer sensitization,³⁰ and dye sensitization.^{31–33} In the latter approach, the excited dye molecule transfers an electron into the conduction band of the semiconductor, leading to the formation of a cationic radical of the dye. The injected electron then reacts with the dioxygen adsorbed on the surface of the metal oxide (MO), and generates active species involved in the process such as O₂^{•-} and dye^{•+}, as shown below:



The subsequent radical chain reactions lead to the degradation and mineralization of a contaminant (R) and concurrently water in the media acts as an electron donor to regenerate the sensitizer dye.³³ For example, Zhao et al. has demonstrated a dye sensitization system incorporating Pt-(dcbpy)Cl₂ (dcbpy = 4,4'-dicarboxy-2,2'-bipyridine) on titania for the visible-light degradation of aqueous organic pollutant 4-chlorophenol in the presence of O₂.³¹ Another study by Sun et al. has also demonstrated that aluminum phthalocyanine loaded on TiO₂ is a good sensitizer for degradation of substituted phenols in aerated aqueous solution under visible-light irradiation.³² Although various organic–inorganic LHNs are found to be active for energy conversion, we come up with an approach to achieve both the eco-friendly VLP process and cost-effective DSSC with a model LHN.

In the first part of this work, a hydrothermally grown, vertically oriented ZnO nanorods (NRs) were sensitized with hematoporphyrin (HP), the first isolated porphyrin that came from the ejection of iron from protoheme and the hydration of the two vinyl side chains to form α -hydroxyethyl groups in their place. To obtain a better understanding of the physical

properties of HP-sensitized ZnO LHNs, we have analyzed the attachment of porphyrin molecules to ZnO surfaces by using FTIR and Raman spectroscopic studies. Upon the binding of HP on ZnO surfaces, the ultrafast charge transfer processes were investigated using steady-state and picosecond-resolved fluorescence techniques. After demonstrating HP–ZnO LHN as an efficient electron transfer mediator, we approached to employ the same nanohybrid in twin applications of efficient VLP process and to the fabrication of stable DSSCs. To the best of our knowledge, this sort of twin applications has not been reported previously by using a less-expensive, more stable, and safer HP–ZnO nanohybrid. To implement this approach, it is essential that rates of heterogeneous electron transfer for the nanohybrid layer be characterized as a function of structural parameters, including surface hydrophilicity, molecular interactions, and nature of anchoring of the chromophores.

2. EXPERIMENTAL SECTION

Analytical-grade chemicals were used for synthesis without further purifications. Fluorine-doped tin oxide (FTO) conducting glass substrates, acquired from Asahi Glass Company, Japan, were cleaned by successive sonication with soap water, acetone, ethanol, and deionized (DI) water for 15 min, each with adequate drying prior to their use.

2.1. Synthesis of ZnO NRs. Zinc acetate dihydrate, Zn(CH₃COO)₂·2H₂O, Merck, zinc nitrate hexahydrate, Zn(NO₃)₂·6H₂O, Sigma–Aldrich, and hexamethylenetetramine, C₆H₁₂N₄, Aldrich, were used as the starting materials for a low temperature hydrothermal synthesis of ZnO NRs on FTO substrates. Detailed processes for the hydrothermal growth of single-crystalline ZnO NRs are described in our previous reports.^{34–36} In brief, ZnO seed layers were initially deposited on cleaned FTO substrates by spray-pyrolysis method at 350 °C using 10 mM zinc acetate aqueous solution. The seeded FTO substrates were then annealed in air at 350 °C for 1 h and used for the hydrothermal growth of the ZnO NRs. A 20-mM aqueous solution of zinc nitrate and hexamethylenetetramine was used as the precursor solution for the ZnO NR growth, which was carried out at 90 °C for 40 h. This leads to the growth of ZnO NRs ca. 4–5 μm in length and 100–200 nm in diameter.^{34,37} During the hydrothermal process, in order to maintain a constant growth rate of the ZnO NRs, the old precursor solution was replaced with a fresh solution in every 5 h. The as-obtained ZnO NR samples were then taken out of the reaction vessel and rinsed thoroughly with DI water thoroughly to remove unreacted residues. Finally, the samples were annealed in air at 350 °C for 1 h prior to the studies in this work.

2.2. Sensitization of HP Dyes on ZnO NR Surface. A 0.5 mM HP C₃₄H₃₈N₄O₆ (Sigma) solution was prepared in anhydrous ethanol under constant stirring at room temperature for 12 h. The sensitization of the ZnO NRs with HP dye was carried out in darkness and at room temperature by dipping the ZnO NR samples into the prepared dye solution for 12 h. After the sensitization process, the ZnO NRs were retracted from the dye solution, rinsed with anhydrous ethanol thoroughly (in order to remove any physisorbed dye molecules), and stored in darkness for further use. The same sensitization conditions were maintained to anchor HP on ZnO surface that was dispersed in ethanol for all the optical measurements.

2.3. Fabrication of DSSCs. For the fabrication of DSSCs, platinum NPs deposited on FTO substrates were used as counter electrodes. The platinum (Pt) NPs were deposited on the FTO substrates by thermal decomposition of 5 mM platinum chloride, H₂PtCl₆·H₂O, Fluka (in isopropanol) at 385 °C for 30 min. The HP-coated ZnO NRs were used as the photoelectrodes and the two electrodes were placed on top of each other with a single layer of 50- μm -thick Surlyn 1702 (Dupont) as a spacer between the two electrodes. A liquid electrolyte composed of 0.5 M lithium iodide (LiI), 0.05 M iodine (I₂), and 0.5 M 4-*tert*-butylpyridine (TBP) in acetonitrile was used as the hole conductor and filled in the interelectrode space by using capillary force, through two small

holes (diameter = 1 mm) predrilled on the counter electrode. Finally, the two holes were sealed by using another piece of Surllyn, to prevent the leakage of electrolyte from the cell. In all our experiments, the active area of the DSSCs was fixed at 0.196 cm².

2.4. Characterization Methods. A scanning electron microscopy (SEM) system (JEOL Model JSM-6301F, operating at 30 kV, working distance = 6.3 mm, magnification = 50000×) was used to study the morphology of as-grown and HP-sensitized ZnO NRs. Powder X-ray diffraction (XRD) patterns were obtained by employing a scanning rate of 0.02° s⁻¹ in the 2θ range from 25° to 60° by PANalytical XPERT-PRO diffractometer equipped with Cu Kα radiation (at 40 mA, 40 kV). For optical experiments, the steady-state absorption and emission are determined with a Shimadzu UV-2450 spectrophotometer and a Jobin-Yvon Fluoromax-3 fluorimeter, respectively. All the photoluminescence transients were measured using the picosecond-resolved time-correlated single photon counting (TCSPC) technique, a commercially available picosecond diode laser-pumped (LifeSpec-ps) fluorescence spectrophotometer from Edinburgh Instruments, U.K. Picosecond excitation pulses from the picosecond diode laser were used at 409 nm with an instrument response function (IRF) of 60 ps. A microchannel-plate-photomultiplier tube (MCP-PMT, Hamamatsu) was used to detect the photoluminescence from the sample after dispersion through a monochromator. For all transients the polarizer on the emission side was adjusted to be at 55° (the magic angle), with respect to the polarization axis of the excitation beam. Curve fitting of observed fluorescence transients were carried out using a nonlinear least-squares fitting procedure to the function

$$X(t) = \int_0^1 E(t')R(t - t') dt'$$

which is comprised of convolution of the IRF ($E(t)$) with a sum of exponentials ($R(t) = A + \sum_{i=1}^N B_i e^{-t/\tau_i}$) with pre-exponential factors (B_i), characteristic lifetimes (τ_i) and a background (A). Relative concentration in a multiexponential decay is expressed as $c_n = (B_n / (\sum_{i=1}^N B_i)) \times 100$. The average lifetime (amplitude-weighted) of a multiexponential decay³⁸ is expressed as

$$\tau_{av} = \sum_{i=1}^N c_i \tau_i$$

Changes in the water contact angle (WCA) on the HP-ZnO surface was studied under normal room light (0.2 sun) and 0.5 sun illumination conditions. For this purpose, 10 μL of water was deposited dropwise on the HP-ZnO substrates and using a digital microscope (Dino-Lite), the change in the WCA was continuously monitored for 10 min under both light conditions. Finally, the WCA after various illumination times was calculated by using ImageJ software.

2.5. Materials and Methods for the VLP Process. For the photocatalysis study, ZnO NRs were grown on glass substrates using microwave irradiation (2.45 GHz) in a commercial microwave oven operated at low mode. Higher photocatalytic activity of the ZnO NRs grown by microwave-assisted hydrothermal process has been previously reported.³⁹ A ZnO nanoparticle seed layer was initially deposited on glass substrates using the same method mentioned in section 2.1. Under the microwave irradiation, ZnO NRs were grown for 4 h using 20 mM aqueous solution of zinc nitrate and hexamethylenetetraamine. As obtained NRs were then rinsed with deionized water (DI) water several times and annealed at 250 °C in air for 1 h. The sensitization of HP was carried out at room temperature, as described in section 2.2.

A 5-μM aqueous solution of MB was then prepared in DI water, which was used as the test contaminant for the photocatalysis test. A homemade flow-device consisting of two glass plates separated by a spacer was used to study the photocatalytic degradation of MB; in which, one of the glass plates of the symmetric device contained the ZnO NRs sensitized with HP dyes. The as-prepared MB solution was then injected through the flow-device and the device placed under a 500-W tungsten-halogen lamp, which was used as the visible-light source in our study. The light was allowed to fall directly on the glass

plate fabricated with HP-ZnO LHNs and, to avoid the heat from the light source, a 20-cm-thick water bath was placed between the light source and the flow device. The position of the device was then adjusted to receive an incoming light power of 75 mW/cm². After 30 min of continuous light irradiation, the photoproduct was collected from the flow device and its optical absorption spectrum was recorded to determine the percentage degradation (% DE) of MB using eq 1:

$$\% DE = \frac{I_0 - I}{I_0} \times 100 \quad (1)$$

where I_0 is the initial absorption intensity of MB at $\lambda_{max} = 664$ nm and I is the absorption intensity after 30 min of continuous photoirradiation.

The VLP process on MB in inert atmosphere was conducted in the similar way as described in the previous section using ZnO NRs sensitized with HP (24 h) as the catalyst media. Prior to the photocatalysis, argon (Ar) gas was passed through the MB solution for 30 min. Similarly, Ar gas was also passed through the flow device for 30 min before injecting aqueous solution of MB. Finally, the solution was injected into the flow device and photocatalysis was conducted for 30 min at light intensity of 75 mW/cm². During the photocatalysis, Ar gas was purged through the flow device. After 30 min, the degraded product from the flow device was collected and its optical absorption was measured to determine the percentage degradation of MB in inert atmosphere using eq 1.

3. RESULTS AND DISCUSSIONS

3.1. Structural Characterization of HP-ZnO LHNs.

Figure 1a shows the photographs of bare (left) and HP-

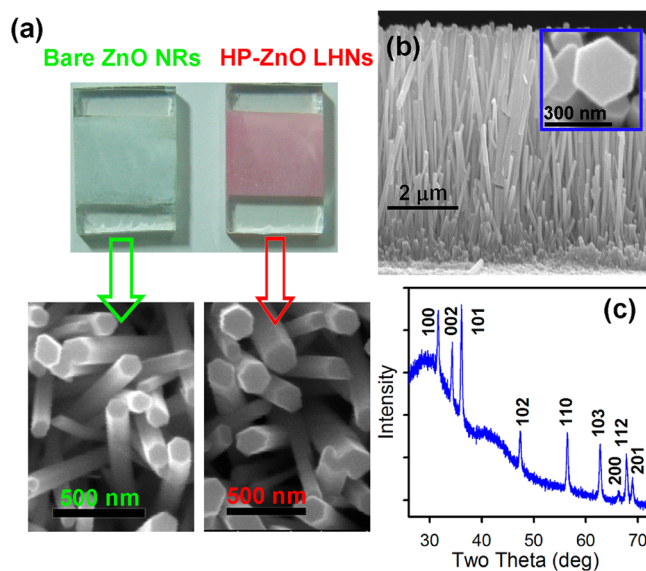


Figure 1. (a) Photographs of bare (left) and HP-sensitized (right) ZnO NRs decorated on FTO plates under daylight and their respective SEM images under the same experimental conditions. (b) Side-view and magnified top-view (inset) SEM images of vertically aligned, hexagonal ZnO NRs. (c) XRD pattern of as-prepared ZnO NRs.

sensitized (right) ZnO NRs decorated on FTO plates under daylight and their respective morphological characterization by SEM images are shown. The contrast difference is clearly noticeable from the two SEM images that were taken under the same experimental conditions for a fair comparison. The side-view SEM image (Figure 1b) indicates the formation of arrays of ZnO NRs with a preferential growth direction along the polar facets in the [0002] direction of the ZnO hexagonal

structure. The NRs growing perpendicular to the substrate are nearly uniform in length ($\sim 4\text{--}5\ \mu\text{m}$) and possess a characteristic hexagonal cross-section with a diameter of $\sim 180\ \text{nm}$ (inset). On the basis of the XRD results (Figure 1c), the crystallographic phase of these ZnO NRs belongs to the wurtzite-type.⁴⁰

3.2. Steady-State Absorption and PL Spectra of HP–ZnO LHNs. The formation of HP–ZnO nanohybrids are characterized by UV–vis spectroscopy. As shown in Figure 2a,

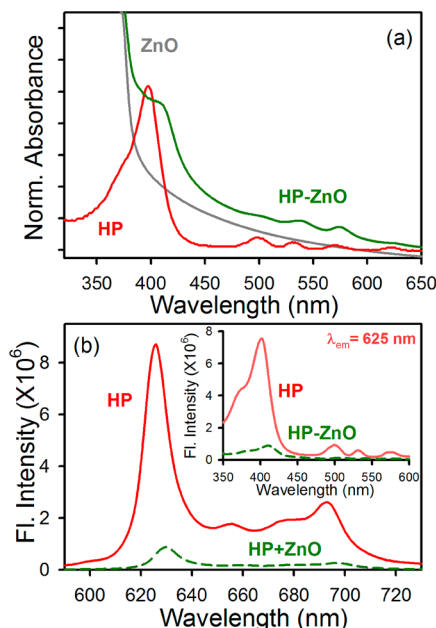


Figure 2. (a) UV-vis absorption spectra of ZnO NRs (gray), HP (red), and HP–ZnO LHNs (green) in ethanol. (b) Room-temperature PL spectra (excitation wavelength was at 409 nm) of bare HP (red) and ZnO-anchored HP (green) are shown. Inset shows the excitation spectra of HP monitored at 625 nm.

ZnO NRs do not show considerable absorption above 410 nm, but the optical absorption increases in the UV region down to 360 nm, which reaches a plateau at $\sim 350\ \text{nm}$. Bare HP exhibits a strong Soret absorption at 396 nm, together with weak Q bands at 500 Q_y ($1\leftarrow 0$), 533 Q_y ($0\leftarrow 0$), 569 Q_x ($1\leftarrow 0$), and 622 nm Q_x ($0\leftarrow 0$).⁴¹ In this respect, the removal of a metal ion from the center of a porphyrin molecule (which is the case in HP) results in the appearance of these four weak bands in the visible region, which have been assigned to the splitting of doubly degenerate states into the vibration components. Relative to HP, HP–ZnO nanohybrid exhibits a 12-nm bathochromic shift and a weaker intensity of the Soret band.⁴² These changes are obvious when compared to the absorption spectrum of HP, and it is reasonable to conclude that HP–ZnO LHNs are formed by the covalent binding of ZnO and anchoring groups of HP rather than only physical adsorption. As shown in Figure 2b, HP molecules are highly emissive as the photogenerated charge carriers undergo radiative recombination. Upon 409-nm laser excitation, the strong emission of HP was suppressed when anchored to ZnO NRs. The dramatic quenching of HP emission by ZnO NRs observed in the composite film is indicative of the fact that radiative decay becomes a minor pathway. The inset of Figure 2b shows the excitation spectra of bare HP and HP–ZnO LHNs monitored at the emission peak (625 nm). The

excitation spectra of HP also show parallel maxima at 400 (Soret), 500, 532, and 574 nm. In addition, the excitation spectra for HP–ZnO LHNs also reveal an $\sim 12\text{-nm}$ bathochromic shift that is in accordance with the observations made from the absorption spectra. Because of the interference of the absorption of ZnO NRs with the excitation wavelength of 409 nm, it is difficult to obtain a quantitative estimate of HP emission quenching which was further established by monitoring the emission decay of HP and HP–ZnO LHNs.

3.3. Picosecond-Resolved Fluorescence Spectra of HP–ZnO LHNs. Using a picosecond-resolved fluorescence technique, we probed the excited-state interactions of HP–ZnO LHNs, which was prepared as discussed in section 2.2. As shown in Figure 3, the fluorescence decay curve of HP was

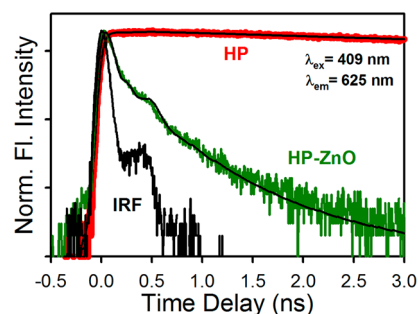


Figure 3. Fluorescence decay profiles of HP–ZnO LHNs (green) and free HP (red) in ethanol.

fitted with single exponential decay, which showed a lifetime of $10.38 \pm 0.06\ \text{ns}$ depicting HP molecules were monomeric in ethanolic solution.⁹ A significant decrease in HP fluorescence lifetime (τ_{avg}) is observed in the presence of ZnO NRs and two fluorescence lifetimes are obtained, which are summarized in Table 1. In particular, a faster component of $0.05 \pm 0.01\ \text{ns}$ generates which contributes nearly 97% of the decay in HP–ZnO composite. Based on the results presented in Figures 2b and 3, we can conclude that an additional nonradiative pathway competes with the fluorescence of excited HP molecules. The apparent rate constant (k_{nr}) is determined for the nonradiative processes by comparing the lifetimes of HP in the absence (τ_0) and the presence (τ) of ZnO NRs, using eq 2.

$$k_{\text{nr}} = \frac{1}{\langle \tau \rangle} - \frac{1}{\langle \tau_0 \rangle} \quad (2)$$

The apparent rate constant for the nonradiative process is estimated to be $(1.66 \pm 0.24) \times 10^{10}\ \text{s}^{-1}$. As reported in previous studies, such k_{nr} values represent electron transfer from lowest unoccupied molecular orbital (LUMO) of HP to the conduction band of ZnO semiconductor and rules out the possibility of self-quenching due to the aggregation of HP molecules on ZnO surface.^{14,43,44} This indicates that the charge injection between excited HP and ZnO NRs is an ultrafast process and it can be modulated by controlling the nature of anchoring of HP to the semiconductor surface.

3.4. FTIR Analysis of HP–ZnO LHNs. The dye used in this study, HP, contains two carboxylic groups, which possesses strong binding ability to the surface of ZnO. Three possible binding modes have been previously proposed for the surface adsorption of carboxylate on metal oxides:^{45–47} (i) the monodentate (esterlike) linkage, (ii) bidentate chelating, and (iii) the bidentate bridging. Infrared vibrational spectroscopy

Table 1. Dynamics of Picosecond-Resolved Luminescence Transients of HP and HP–ZnO LHNs^a

sample	τ_1 (ns)	τ_2 (ns)	τ_{avg} (ns)	k_{nr} ($\times 10^{10} \text{ s}^{-1}$)
HP (bare)		10.38 ± 0.06 (100%)	10.38 ± 0.06	
HP–ZnO	0.05 ± 0.01 (97%)	0.47 ± 0.02 (3%)	0.06 ± 0.01	1.66 ± 0.24

^aThe emission (monitored at 625 nm) was detected with 409-nm laser excitation. k_{nr} represents nonradiative rate constant. Numbers in the parentheses indicate relative weightages.

usually provides a powerful tool to distinguish these binding modes. Generally, the frequency difference between the antisymmetric and symmetric stretching vibration ($\Delta = \nu_{\text{as}} - \nu_{\text{s}}$) of carboxylate group is in the order of $\Delta(\text{monodentate}) > \Delta(\text{ionic}) \approx \Delta(\text{bridging}) > \Delta(\text{bidentate})$. For the pure dye, the stretching vibration band of carboxylic group is located at 1714 cm^{-1} , as shown in Figure 4a. After coordinating to ZnO surface,

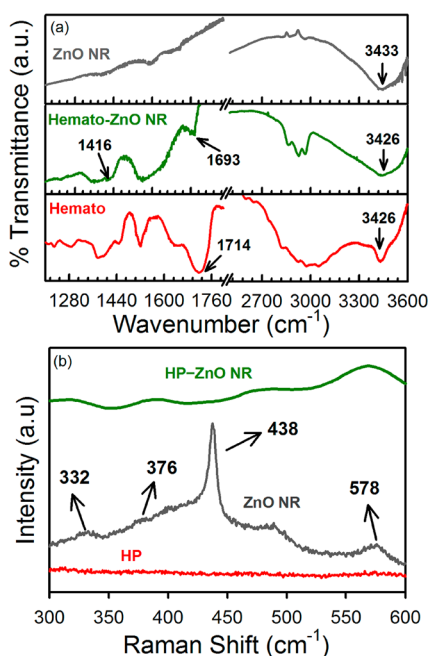


Figure 4. (a) FTIR and (b) Raman spectra of HP (red), ZnO NRs (gray), and HP–ZnO LHNs (green).

this vibration band splits into two bands (1693 and 1416 cm^{-1} , respectively). The band located at 1693 cm^{-1} is ascribed to the antisymmetric stretching vibration of coordinated carboxylate group, while the shoulder band at 1416 cm^{-1} corresponds to the symmetric vibration. Therefore, the Δ value estimated for HP adsorbed on the pure ZnO is found to be 277 cm^{-1} ($1693 - 1416 = 277 \text{ cm}^{-1}$), which is a much larger value and suggests that the binding mode of HP on ZnO is dominantly the monodentate esterlike linkage. In a previous study, Zhao et al also reported monodentate binding of Rhodamine B dyes with TiO_2 and Al(III) -modified TiO_2 nanoparticles, with a Δ value of 262 and 281 cm^{-1} , respectively.⁴⁸

3.5. Raman Spectra of HP–ZnO LHNs. The Raman spectra collected from HP, ZnO NRs, and HP–ZnO LHNs in the wavenumber region of $300\text{--}600 \text{ cm}^{-1}$ are shown in Figure 4b. As evidenced from the figure, HP molecules do not show an obvious peak in the experimental range. The Raman spectrum of the ZnO NR arrays exhibits four vibration peaks at 332 , 376 , 438 , and 578 cm^{-1} thus indicating the presence of wurtzite structure.^{9,49} The peaks at 376 and 578 cm^{-1} correspond to the polar transverse A_1 and longitudinal E_1 optical phonon mode,

respectively; the peak at 332 cm^{-1} is attributed to the $E_2^{\text{high}} - E_2^{\text{low}}$ mode; and the strong peak at 438 cm^{-1} can be assigned to the nonpolar optical phonon E_2 mode of the ZnO NRs at high frequency, which is associated with oxygen deficiency.^{9,50} After binding HP to ZnO, the E_2 mode characteristic band of ZnO, associated to defect centers, is significantly perturbed. This is indicative of the passivation of ZnO surface states upon HP assembly. The presence of other characteristic bands indicates good retention of ZnO wurtzite structure and crystal shape during the sensitization of ZnO NRs with HP.

3.6. Visible-Light Photocatalysis of MB by HP–ZnO LHNs. In order to apply our findings into a model application, we designed a flow device consisting of two glass plates (separated by a spacer), as illustrated in section 2.5. The research was aimed to clarify (1) the efficiency of the HP–ZnO LHNs for the degradation of dye pollutants under visible-light irradiation, (2) the effect of dye-sensitization time on the degradation efficiency, and (3) the mechanism of catalytic enhancement of photodegradation of dye pollutants under visible irradiation. As dye-sensitized systems solely rely on trapped conduction band electrons to reduce dioxygen to superoxide, many dyes simply cannot survive this severe oxidative stress.^{30–32,51–53} The optical response of the visible-light source was found to be effective in the region of $420\text{--}950 \text{ nm}$ with a maximum intensity at 620 nm (see Figure 5b, inset).

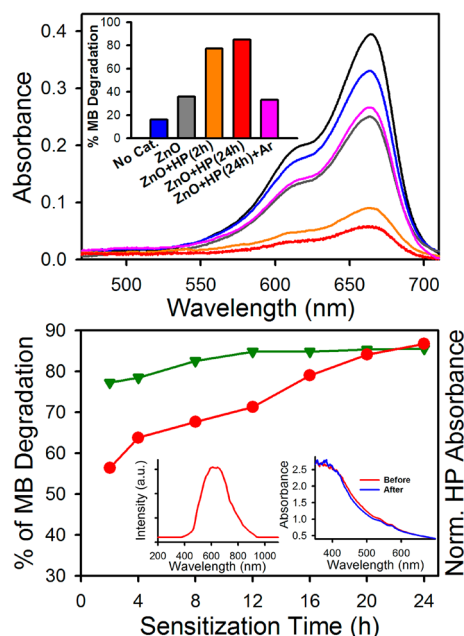


Figure 5. (a) UV–vis spectral changes of aqueous solution of MB in the absence and the presence of ZnO and HP–ZnO LHNs, under visible-light irradiation. (b) Dependence of photocatalytic activity on the dye-sensitization time (inset to the left shows the optical response of our visible light source, and inset to the right shows the absorbance of HP-sensitized (24 h) ZnO LHNs (on a quartz plate) before and after the photocatalysis process).

The present work identifies a highly stable photocatalytic material (HP–ZnO), which promotes the visible-light-sensitized ($\lambda > 420$ nm) decomposition of aqueous MB, a representative organic pollutant, in the presence of air without the need for any undesirable sacrificial electron donors to promote regeneration of surface-bound sensitizer molecules. Figure 5a shows the change of absorption spectra of MB solution when exposed to visible light in the absence and presence of ZnO NRs and HP–ZnO LHNs at two extreme sensitization times, indicating the decolorization of MB during photoassisted reaction. The histogram (inset) clearly shows that degradation efficiency markedly enhanced in the presence of HP–ZnO LHNs, and it is also dependent on the HP sensitization time that reaches $\sim 85\%$ after 24 h of HP sensitization.

In order to confirm that the HP–ZnO-induced VLP process occurs via the formation of reactive oxygen species (ROS), we performed MB photodegradation in an argon (Ar) atmosphere. Under deaerated conditions, a suppression of $O_2^{\cdot -}$ radical production occurs and the reducing action of CB electrons is decreased, because of the inhibition of the degradation efficiency of HP–ZnO LHNs (24 h) from 85% to 33%. In this respect, Sun and Xu had used TiO_2 –aluminum phthalocyanine nanohybrids to degrade water pollutant 4-chlorophenol where the catalyst capacity toward O_2 adsorption in aqueous solution was found to be a predominant factor.³² For further understanding of the effect of dye-sensitization time on VLP activity, many HP–ZnO substrates were prepared with different sensitization periods of 2, 4, 8, 12, 16, 20, and 24 h. Figure 5b shows that the absorption of HP–ZnO LHNs is quite expectedly increased with increasing sensitization times, and the catalytic activity also increased due to the higher adsorption of sensitizing dye on ZnO surface which was found to be saturated after 12 h of sensitization time and remain constant thereafter. It is worth noting that the increment of HP concentration must lower the possibility of MB to attach to ZnO surface that would lead to a deterioration of degradation efficiency for increasing HP sensitization time. However, the reverse output again reveals that the bleaching process is followed by ROS formation that are generated at the ZnO surface and subsequently transported to the MB layer. Therefore, the remote bleaching is not a simple reduction of MB to its leuco form at the surface of ZnO; rather, MB is probably oxygenated or decomposed. This sort of remote bleaching of MB in the gas phase is well-specified in the literature.^{54,55} In addition, we have verified the photostability of HP–ZnO LHNs by measuring the absorbance of HP–ZnO film (on a quartz plate) prior to and after the completion of photocatalysis reaction. As shown in the inset of Figure 5b, after passing 2 mL aqueous solution of MB through the flow device and 30 min of continuous light irradiation, it was found that a negligible amount of HP leached out from the quartz plate.

3.7. Water Contact-Angle Measurements on HP–ZnO LHNs. The spreading of water on solid substrates is usually quantified through the contact angle, which positively characterizes the hydrophilicity and determines the biocompatibility of the materials.⁵⁶ The contact angle measurements were done on HP–ZnO films fabricated on a glass plate, under 0.5 sun and normal room-light intensity (0.2 sun). As shown in Figure 6, initially HP–ZnO film shows a water contact angle of 129.1° , which gradually reduces with increasing time of irradiation. After 10 min of experimental time window, it is found that HP–ZnO becomes more hydrophilic when

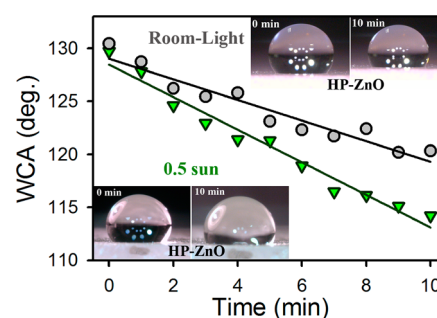
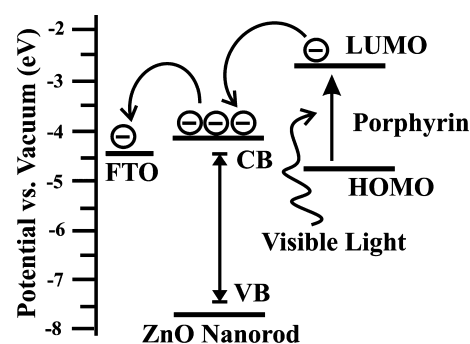


Figure 6. Water contact-angle measurements on HP–ZnO modified substrates under the illumination of 0.5 sun and normal room light. Insets show their respective photographs.

irradiated under 0.5 sun illumination, compared to normal room light. This suggests that the electron–hole (e–h) pair generation occurs at a much faster rate when higher-intensity light is incident on the HP–ZnO surface. Upon illumination, HP will inject electrons to the ZnO conduction band which may get trapped in the surface defect states (mainly oxygen vacancy centers) if there is no external force to sweep these electrons out. As a consequence, the surface trapped electrons will build up a hydrophilic surface until an equilibrium state of release is reached. Therefore, higher light intensity would facilitate the photocatalysis of a water contaminant in LHNs. The insets show their corresponding photographs.

3.8. Optimized DSSC Performance. Photoelectrochemical measurements^{37,57} were performed in a standard two-compartment cell, in acetonitrile containing 0.5 M LiI and 0.01 M I_2 as redox electrolyte and FTO/ZnO/HP as working electrode, while Pt/FTO was the counter electrode. Shown in Scheme 1 is the energy level alignment of ZnO NRs and

Scheme 1. Schematic Energy Level Diagram and Electron-Transfer Path from Porphyrin Dyes to ZnO



porphyrin dyes, to demonstrate the electron transfer pathway in the photocurrent system. Previous studies have estimated that the conduction band (CB) and the valence band (VB) of the ZnO NRs are located at -4.2 and -7.6 eV,⁹ and the LUMO and the highest occupied molecular orbital (HOMO) of porphyrin dyes are located at approximately -2.75 and -4.75 eV, respectively.^{58,59} Upon visible-light irradiation, the electrons in HP molecules are injected to the CB of ZnO and consequently transported to the FTO plates, leading to a photocurrent. The photocurrent density–voltage (J – V) curves of the devices measured under AM 1.5 irradiation (100 mW cm^{-2}) are shown in Figure 7a, and the detailed photovoltaic parameters are summarized in Table 2. The fill factor (FF) and

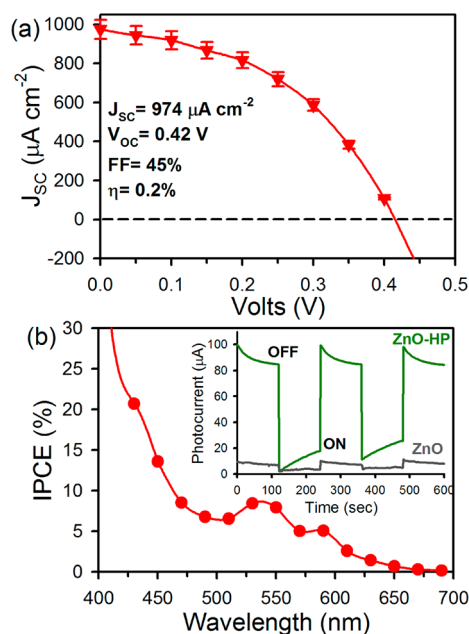


Figure 7. (a) Photocurrent–voltage (J – V) characteristics and (b) incident photon-to-current conversion efficiency (IPCE) spectra for HP-sensitized ZnO NR-based DSSCs. Inset shows photocurrent responses of ZnO NRs (gray) and HP–ZnO LHN (green) modified FTO electrode under the bias voltage of 2.5 V. The photocurrent was measured across the thickness of the films with an incident power of 25 mW cm^{-2} from a halogen light source.

Table 2. Device Performance^a of the HP-Sensitized DSSCs

device	V_{OC} (V)	J_{SC} ($\mu\text{A}/\text{cm}^2$)	FF (%)	η (%)
HP–ZnO	0.42 ± 0.02	974 ± 48	45 ± 6	0.20 ± 0.02
N719–ZnO (control)	0.69 ± 0.05	620 ± 33	30 ± 5	0.13 ± 0.01

^aShort-circuit photocurrent densities (J_{SC}/cm^2), open-circuit voltage (V_{OC}), fill factor (FF), and efficiency (η). The control experiment with a N719 dye-sensitized system is provided from our previous report (ref 37).

power conversion efficiency (η) of the solar cells are determined from eqs 3 and 4:

$$FF = \frac{V_M J_M}{V_{OC} J_{SC}} \quad (3)$$

$$\eta = \frac{V_{OC} J_{SC} FF}{P_{in}} \quad (4)$$

where V_M and J_M are the voltage and current density at the maximum power output, respectively, and P_{in} is the intensity of the incident light (100 mW cm^{-2}). The short-circuit photocurrent density (J_{SC}), open-circuit photovoltage (V_{OC}), and FF of a HP-sensitized cell with the iodine-based electrolyte are $\sim 974 \pm 48 \mu\text{A cm}^{-2}$, $0.42 \pm 0.02 \text{ V}$, and $45\% \pm 6\%$, respectively, with an overall conversion efficiency (η) of $0.20\% \pm 0.02\%$. Note that a well-recognized ruthenium-based solar cell dye N719 provides η of 0.13 ± 0.01 under the same experimental conditions, which is comparable with HP–ZnO-based DSSCs.³⁷

The incident photon-to-current conversion efficiency (IPCE) for HP-sensitized DSSCs is shown in Figure 7b. The IPCE, which is defined as the number of electrons collected per

incident photon, was evaluated from short-circuit photocurrent (J_{sc}) measurements at different wavelengths (λ), and the IPCE was calculated using eq 5:

$$IPCE (\%) = \frac{1240 \times J_{SC} (\text{A}/\text{cm}^2)}{\lambda (\text{nm}) \times P (\text{W}/\text{cm}^2)} \times 100 \quad (5)$$

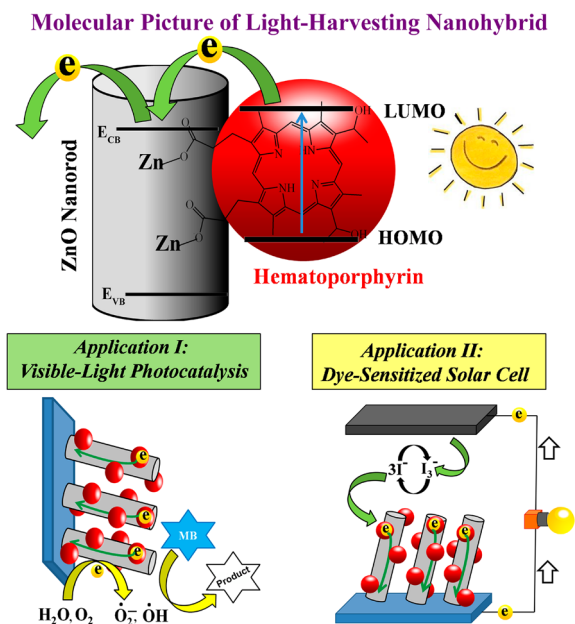
where P is the incident light power. The IPCE spectra are found to closely resemble the characteristic absorbance spectra of HP (Figure 2a), which exhibit peaks near 530 and 580 nm, because of the Q bands, and reaches a maximum value of $\sim 30\%$ at the Soret region ($\sim 400 \text{ nm}$), signifying that the HP sensitizers on the photoanode surface are indeed responsible for photocurrent generation. In this respect, a recent study employed a noncovalent double-decker binding strategy to construct functional supramolecular single-wall carbon nanotubes–zinc porphyrin hybrids where a maximum of 12% IPCE has been achieved without any modification of porphyrin side-chains.⁶⁰

The photoconductivity measurements^{37,57,61} of bare ZnO and HP-modified ZnO thin films are also performed in order to better understand the photocurrent response of the nano-hybrids. At a fixed bias voltage of 5 V, the photocurrent across the thickness of the films were measured by using FTO as one of the electrodes and a small (4-mm-diameter) drop of mercury (Hg) on top of the film as a counter electrode. The light source (intensity 25 mW cm^{-2}) was turned on and off every 20 s, and the obtained current values were continuously recorded using a programmable multimeter (Gwinstek Model GDM-396). Inset of Figure 7b shows the photocurrent response for the ZnO NR and HP–ZnO thin films, where an improved photocurrent was observed for the HP-modified ZnO thin film ($\sim 100 \mu\text{A}$) under illuminated condition compared to the bare ZnO NR thin film ($\sim 10 \mu\text{A}$).

4. CONCLUSION

In conclusion, hematoporphyrin (HP) has been conjugated onto covalently functionalized ZnO NRs, forming electron donor–acceptor HP–ZnO nano-hybrids, which are being established as potential light-harvesting materials, as represented in Scheme 2. The new hybrid nanomaterial has been methodically characterized with the aid of standard microscopic and optical techniques. The FTIR and Raman scattering studies confirm the formation of HP–ZnO nano-hybrid through the monodentate binding of ZnO and carboxylic groups of HP rather than simply physical adsorption. Steady-state and picosecond-resolved fluorescence measurements reveal efficient quenching of HP fluorescence in the HP–ZnO nano-hybrid, suggesting that photoinduced charge transfer takes place from LUMO of HP to the conduction band (CB) of ZnO. Utilizing this phenomenon, a new dye-sensitized system, incorporating HP on ZnO, is realized for the photodegradation of aqueous organic pollutants under visible-light irradiation. Finally, a photoelectrochemical cell is constructed based on HP sensitization onto nanostructured ZnO at fluorine-doped tin oxide (FTO) plates. The FTO/ZnO/HP electrode revealed prompt, stable and reproducible photocurrent and photovoltage, with incident photon-to-current conversion efficiency (IPCE) values as large as 30%, without the application of bias voltage. The present work demonstrates the exciting potential of porphyrins as light-harvesting green dyes that can simultaneously be used in visible-light photocatalysis and

Scheme 2. Schematic Representation of a Model Light-Harvesting Nanohybrid (LHN) Depicting Covalently Functionalized ZnO NRs with Sensitizing Dye, Hematoporphyrin (HP)^a



^aThe scheme illustrates the typical absorption process for visible light in the LHNs: light is absorbed by the sensitizing dye HP, transferring an electron into the conduction band (CB) of ZnO. The trapped electron in ZnO is exploiting dual vital applications of using HP–ZnO nanohybrid as a model light-harvesting material: (I) visible-light photocatalysis and (II) dye-sensitized solar cell.

photovoltaics, and further work is underway in our laboratories to develop this.

AUTHOR INFORMATION

Corresponding Author

*E-mail: skpal@bose.res.in.

Notes

The authors declare no competing financial interest.

ACKNOWLEDGMENTS

S.S. thanks UGC (India) and A.M. thanks CSIR (India) for fellowships. We thank DST (India) for financial grants (No. DST/TM/SERI/2k11/103). T.B. thanks the Sheikh Saqr Al Qasimi Graduate Research Fellowship.

REFERENCES

- (1) Chen, C. Y.; Wang, M.; Li, J. Y.; Pootrakulchote, N.; Alibabaei, L.; Ngoc-le, C.; Decoppet, J. D.; Tsai, J. H.; Grätzel, C.; Wu, C. G.; et al. *ACS Nano* **2009**, *3*, 3103–3109.
- (2) Nazeeruddin, M. K.; Klein, C.; Liska, P.; Grätzel, M. *Coord. Chem. Rev.* **2005**, *249*, 1460–1467.
- (3) Ku, C.; Wu, J. *Appl. Phys. Lett.* **2007**, *91*, 093117.
- (4) Wanga, Z.; Kawachib, H.; Kashimab, T.; Arakawa, H. *Coord. Chem. Rev.* **2004**, *248*, 1381–1389.
- (5) Wang, C. L.; Lan, C. M.; Hong, S. H.; Wang, Y. F.; Pan, T. Y.; Chang, C. W.; Kuo, H. H.; Kuo, M. Y.; Diau, E. W. G.; Lin, C. Y. *Energy Environ. Sci.* **2012**, *5*, 6933–6940.
- (6) Wu, S. L.; Lu, H. P.; Yu, H. T.; Chuang, S. H.; Chiu, C. L.; Lee, C. W.; Diau, E. W. G.; Yeh, C. Y. *Energy Environ. Sci.* **2010**, *3*, 949–955.

- (7) Lee, C. W.; Lu, H. P.; Lan, C. M.; Huang, Y. L.; Liang, Y. R.; Yen, W. N.; Liu, Y. C.; Lin, Y. S.; Diau, E. W. G.; Yeh, C. Y. *Chem.—Eur. J.* **2009**, *15*, 1403–1412.
- (8) Drain, C. M.; Varotto, A.; Radivojevic, I. *Chem. Rev.* **2009**, *109*, 1630–1658.
- (9) Tu, W.; Lei, J.; Wang, P.; Ju, H. *Chem.—Eur. J.* **2011**, *17*, 9440–9447.
- (10) Liu, Y.; Zhang, Y.; Wang, S.; Pope, C.; Chen, W. *Appl. Phys. Lett.* **2008**, *92*, 143901.
- (11) Shrestha, M.; Si, L.; Chang, C. W.; He, H.; Sykes, A.; Lin, C. Y.; Diau, E. W. G. *J. Phys. Chem. C* **2012**, *116*, 10451–10460.
- (12) Campbell, W. M.; Jolley, K. W.; Wagner, P.; Wagner, K.; Walsh, P. J.; Gordon, K. C.; Schmidt-Mende, L.; Nazeeruddin, M. K.; Wang, Q.; Grätzel, M.; et al. *J. Phys. Chem. C* **2007**, *111*, 11760–11762.
- (13) Wang, Q.; Campbell, W. M.; Bonfantani, E. E.; Jolley, K. W.; Officer, D. L.; Walsh, P. J.; Gordon, K.; Humphry-Baker, R.; Nazeeruddin, M. K.; Grätzel, M. *J. Phys. Chem. B* **2005**, *109*, 15397–15409.
- (14) Saarenpaa, H.; Sariola-Leikas, E.; Perros, A. P.; Kontio, J. M.; Efimov, A.; Hayashi, H.; Lipsanen, H.; Imahori, H.; Lemmetyinen, H.; Tkachenko, N. V. *J. Phys. Chem. C* **2012**, *116*, 2336–2343.
- (15) Xu, Y.; Liu, Z.; Zhang, X.; Wang, Y.; Tian, J.; Huang, Y.; Ma, Y.; Zhang, X.; Chen, Y. *Adv. Mater.* **2009**, *21*, 1275–1279.
- (16) Pagona, G.; Zervaki, G. E.; Sandanayaka, A. S. D.; Ito, O.; Charalambidis, G.; Hasobe, T.; Coutsolelos, A. G.; Tagmatarchis, N. *J. Phys. Chem. C* **2012**, *116*, 9439–9449.
- (17) Gong, X.; Milic, T.; Xu, C.; Batteas, J. D.; Drain, C. M. *J. Am. Chem. Soc.* **2002**, *124*, 14290–14291.
- (18) Abdul, S. A.; Cui, J. B. *J. Phys. Chem. C* **2012**, *116*, 9433–9438.
- (19) Subbaiyan, N. K.; Maligaspe, E.; D'Souza, F. *ACS Appl. Mater. Interfaces* **2011**, *3*, 2368–2376.
- (20) Stromberg, J. R.; Marton, A.; Kee, H. L.; Kirmaier, C.; Diers, J. R.; Muthiah, C.; Taniguchi, M.; Lindsey, J. S.; Bocian, D. F.; Meyer, G. J.; et al. *J. Phys. Chem. C* **2007**, *111*, 15464–15478.
- (21) Yella, A.; Lee, H. W.; Tsao, H. N.; Yi, C.; Chandiran, A. K.; Nazeeruddin, M. K.; Diau, W. G. E.; Yeh, C. Y.; Zakeeruddin, S. M.; Grätzel, M. *Science* **2011**, *334*, 629–634.
- (22) Zhao, L.; Hu, L.; Fang, X. *Adv. Funct. Mater.* **2012**, *22*, 1551–1566.
- (23) Chen, C. C.; Li, X. Z.; Ma, W. H.; Zhao, J. C.; Hidaka, H.; Serpone, N. *J. Phys. Chem. B* **2002**, *106*, 318–324.
- (24) Asahi, R.; Morikawa, T.; Ohwaki, T.; Aoki, K.; Taga, Y. *Science* **2001**, *293*, 269–271.
- (25) Lu, N.; Quan, X.; Li, J.; Chen, S.; Yu, H.; Chen, G. *J. Phys. Chem. C* **2007**, *111*, 11836–11842.
- (26) Li, X. Z.; Li, F. B. *Environ. Sci. Technol.* **2001**, *35*, 2381–2387.
- (27) Zhang, Z.; Wang, W.; Wang, L.; Sun, S. *ACS Appl. Mater. Interfaces* **2012**, *4*, 593–597.
- (28) Jiang, J.; Zhang, X.; Sun, P.; Zhang, L. *J. Phys. Chem. C* **2011**, *115*, 20555–20564.
- (29) Li, G. S.; Zhang, D. Q.; Yu, J. C. *Environ. Sci. Technol.* **2009**, *43*, 7079–7085.
- (30) Zhang, H.; Zong, R. L.; Zhao, J. C.; Zhu, Y. F. *Environ. Sci. Technol.* **2008**, *42*, 3803–3807.
- (31) Zhao, W.; Sun, Y.; Castellano, F. N. *J. Am. Chem. Soc.* **2008**, *130*, 12566–12567.
- (32) Sun, Q.; Xu, Y. *J. Phys. Chem. C* **2009**, *113*, 12387–12394.
- (33) Bae, E.; Choi, W. *Environ. Sci. Technol.* **2003**, *37*, 147–152.
- (34) Baruah, S.; Dutta, J. *J. Cryst. Growth* **2009**, *311*, 2549–2554.
- (35) Baruah, S.; Dutta, J. *J. Sol-Gel Sci. Technol.* **2009**, *50*, 456–464.
- (36) Fang, X.; Hu, L.; Ye, C.; Zhang, L. *Pure Appl. Chem.* **2010**, *82*, 2185–2198.
- (37) Sarkar, S.; Makhal, A.; Lakshman, K.; Bora, T.; Dutta, J.; Pal, S. *K. J. Phys. Chem. C* **2012**, *116*, 14248–14256.
- (38) Lakowicz, J. R. *Principles of Fluorescence Spectroscopy*, 2nd Edition; Kluwer Academic/Plenum: New York, 1999.
- (39) Baruah, S.; Mahmood, M. A.; Myint, M. T. Z.; Bora, T.; Dutta, J. *Beilstein J. Nanotechnol.* **2010**, *1*, 14–20.
- (40) Liu, B.; Zeng, H. C. *J. Am. Chem. Soc.* **2003**, *125*, 4430–4431.

- (41) Srivastava, R. C.; Anand, V. D.; Carper, W. R. *Appl. Spectrosc.* **1973**, *27*, 444–449.
- (42) Castellero, P.; Sanchez-Valencia, J. R.; Cano, M.; Pedrosa, J. M.; Roales, J.; Barranco, A.; Gonzalez-Elipe, A. R. *ACS Appl. Mater. Interfaces* **2010**, *2*, 712–721.
- (43) Hasobe, T.; Saito, K.; Kamat, P. V.; Troiani, V.; Qui, H.; Solladie, N.; Kim, K. S.; Park, J. K.; Kim, D.; D'Souza, F.; et al. *J. Mater. Chem.* **2007**, *17*, 4160–4170.
- (44) Cheng, H. M.; Hsieh, W. F. *Nanotechnology* **2010**, *21*, 485202.
- (45) Weng, Y. X.; Li, L.; Liu, Y.; Wang, L.; Yang, G. Z. *J. Phys. Chem. B* **2003**, *107*, 4356–4363.
- (46) Boettcher, S. W.; Bartl, M. H.; Hu, J. G.; Stucky, G. D. *J. Am. Chem. Soc.* **2005**, *127*, 9721–9730.
- (47) Deacon, G. B.; Phillips, R. J. *Coord. Chem. Rev.* **1980**, *33*, 227–250.
- (48) Zhao, D.; Chen, C.; Wang, Y.; Ma, W.; Zhao, J.; Rajh, T.; Zang, L. *Environ. Sci. Technol.* **2008**, *42*, 308–314.
- (49) Zhang, Y.; Jia, H.; Wang, R.; Chen, C.; Luo, X.; Yu, D.; Lee, C. *Appl. Phys. Lett.* **2003**, *83*, 4631–4633.
- (50) Jiang, P.; Zhou, J. J.; Fang, H. F.; Wang, C. Y.; Wang, Z. L.; Xie, S. S. *Adv. Funct. Mater.* **2007**, *17*, 1303–1310.
- (51) Liang, H. C.; Li, X. Z. *Appl. Catal., B* **2009**, *86*, 8–17.
- (52) Wang, D. S.; Zhang, J.; Luo, Q. Z.; Li, X. Y.; Duan, Y. D.; An, J. *J. Hazard. Mater.* **2009**, *169*, 546–550.
- (53) Chen, C.; Zhao, W.; Li, J.; Zhao, J.; Hidaka, H.; Serpone, N. *Environ. Sci. Technol.* **2002**, *36*, 3604–3611.
- (54) Tatsuma, T.; Tachibana, S. I.; Miwa, T.; Tryk, D. A.; Fujishima, A. *J. Phys. Chem. B* **1999**, *103*, 8033–8035.
- (55) Tatsuma, T.; Tachibana, S.; Fujishima, A. *J. Phys. Chem. B* **2001**, *105*, 6987–6992.
- (56) Liu, Y.; Lin, Z.; Lin, W.; Moon, K. S.; Wong, C. P. *ACS Appl. Mater. Interfaces* **2012**, *4*, 3959–3964.
- (57) Sarkar, S.; Makhil, A.; Bora, T.; Baruah, S.; Dutta, J.; Pal, S. K. *Phys. Chem. Chem. Phys.* **2011**, *13*, 12488–12496.
- (58) Liu, D.; Wu, W.; Qiu, Y.; Yang, S.; Xiao, S.; Wang, Q. Q.; Ding, L.; Wang, J. *Langmuir* **2008**, *24*, 5052–5059.
- (59) Kee, H. L.; Kirmaier, C.; Tang, Q.; Diers, J. R.; Muthiah, C.; Taniguchi, M.; Laha, J. K.; Ptaszek, M.; Lindsey, J. S.; Bocian, D. F.; et al. *Photochem. Photobiol.* **2007**, *83*, 1125–1143.
- (60) Sandanayaka, A. S. D.; Subbaiyan, N. K.; Das, S. K.; Chitta, R.; Maligaspe, E.; Hasobe, T.; Ito, O.; D'Souza, F. *Chem. Phys. Chem.* **2011**, *12*, 2266–2273.
- (61) Hu, L.; Yan, J.; Liao, M.; Xiang, H.; Gong, X.; Zhang, L.; Fang, X. *Adv. Mater.* **2012**, *24*, 2305–2309.